Supporting Information

Photothermal catalytic co-oxidation of toluene and acetone over core-shell structured GCS@MnO_2

Linbo Qin[1, 2], Huiqi Tan[1], Tengteng Zhang[1], Bo Zhao[1], Jun Han[1, 2]

[1]College of Resources and Environment Engineering, Wuhan University of Science and Technology, Wuhan, 430081, P.R. China

[2]Wuhan Institute of Photochemistry and Technology, Wuhan, 430080, P.R. China

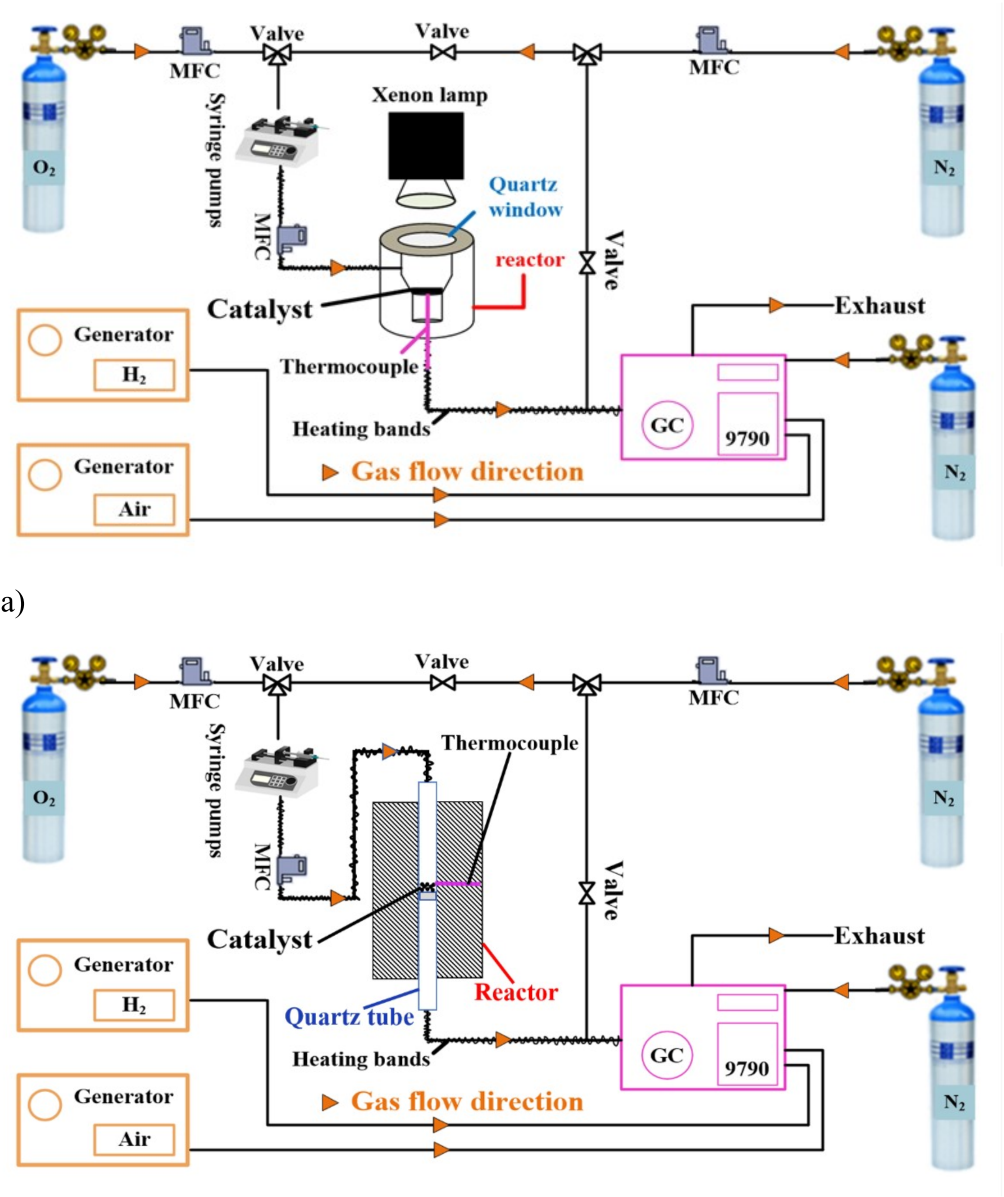

(a)

(b)

Fig. S1 Reaction system: (a) PTCO; (b) TCO

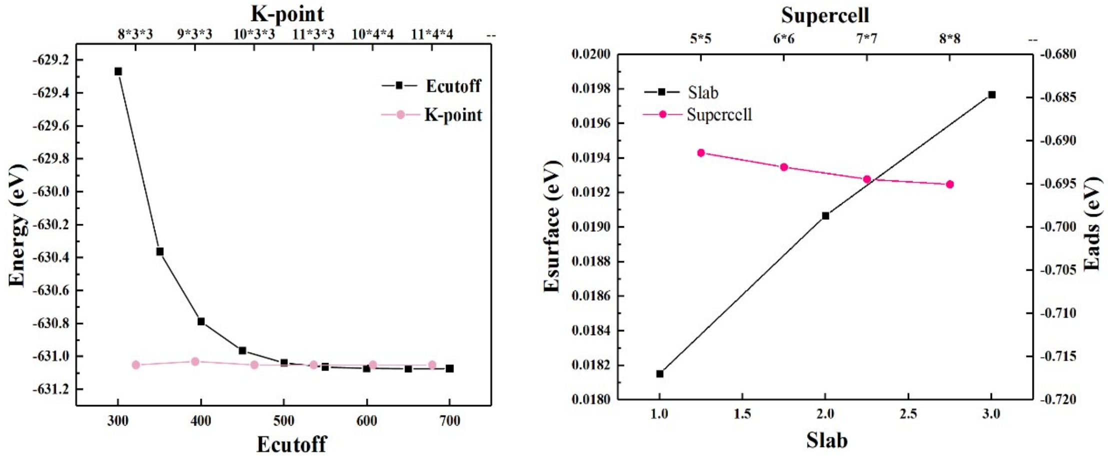

(a) (b)

Fig. S2 Model test: (a) Cutoff energy and K value; (b) CSurface energy and the toluene adsorption energy

Characterization of all samples:

The characterization data for control samples GCS@MnO_2-2, GCS@MnO_2-4, GCS@MnO_2-6, GCS@MnO_2-8, and GCS@MnO_2-10 are provided in Fig. S3–S6 and Table S1–S3. **Notably, the GCS@MnO_2-6 catalyst (denoted as GCS@MnO_2) is the primary focus of this study.** Fig. S3(a) presents the N_2 adsorption-desorption isotherms and pore size distributions of the GCS@MnO_2-x catalysts. The GCS isotherm displays typical Type IV characteristics with an H2-type hysteresis loop, indicative of a uniform mesoporous structure. BJH analysis reveals a primary pore size distribution concentrated within 2–4 nm. Notably, while GCS@MnO_2-x also exhibits a Type IV isotherm, an H3-type hysteresis loop emerges at higher relative pressure (P/P_0). This feature is attributed to capillary condensation within mesopores [1]. Pore size distribution analysis further indicates that this H3-type hysteresis originates from the layered slit-pore structure formed by MnO_2 nanosheets on the GCS surface [2]. Structural parameters summarized in Table 1 demonstrate that the specific surface area (S_{BET}) of GCS@MnO_2-x catalysts is substantially lower than that of pristine GCS. The S_{BET} values follow the order: GCS (522.9 $m^2 \cdot g^{-1}$) > GCS@MnO_2-2 (242.2 $m^2 \cdot g^{-1}$) > GCS@MnO_2-4 (216.3 $m^2 \cdot g^{-1}$) >GCS@MnO_2-6 (171.1 $m^2 \cdot g^{-1}$) > GCS@MnO_2-8 (57.9 $m^2 \cdot g^{-1}$) > GCS@MnO_2-10 (47.6 $m^2 \cdot g^{-1}$) > MnO_2 (45.8 $m^2 \cdot g^{-1}$). Increasing $KMnO_4$ concentration correlates with a progressive reduction in S_{BET}, suggesting interactions between GCS and Mn species. Critically, the incorporation of GCS significantly enhances the S_{BET} of GCS@MnO_2-x relative to pure MnO_2 [3]. This expanded surface area facilitates enhanced mass transport and increased active site availability, thereby promoting VOC adsorption and oxidation [1].

The XRD patterns of the GCS@MnO_2-x catalysts are shown in Fig. S3 (c-d). As shown in Fig. S3 (c), the characteristic diffraction peak of the (002) crystal plane of

GCS appears at 26.5 °, which is highly consistent with the graphite layered structure observed by HRTEM, indicating its highly ordered graphitization characteristics. In addition, a weak diffraction peak of the (100) crystal plane of graphite oxide appears at 42.3 °, confirming that GCS has been successfully graphitized [4]. As shown in Fig. S3(d), the XRD spectrum of GCS@MnO_2-2 shows obvious diffraction peaks of MnOOH at 24.1 °, 33.5 °, 35.6 °, 36.1 °, 51.2 °, 52.6 °, 54.4 °, 61.2 ° and 65.8 ° (JCPDS No. 41–1379). When the concentration of $KMnO_4$ exceeds 4 mmol, it is found that the diffraction peaks at 11.5 °, 24.8 °, 36.9 ° and 66.3 ° correspond to δ-MnO_2 (JCPDS No. 80–1098), and the characteristic peaks of MnOOH phase disappear, indicating that the loading amount has a significant regulatory effect on the crystal form of Mn oxides. Further analysis shows that compared with other GCS@MnO_2-x samples, the diffraction peak width of δ-MnO_2 in GCS@MnO_2-6 increases significantly, indicating a decrease in its crystallinity and an increase in pore channels, which is beneficial to charge transfer [5]. In addition, compared with pure δ-MnO_2, the diffraction peaks of δ-MnO_2 in GCS@MnO_2-x shift towards a higher angle, indicating that lattice distortion is caused by the presence of oxygen vacancies in GCS@MnO_2-x [4].

The structure of the synthesized GCS@MnO_2-x catalysts was characterized using Raman spectroscopy, with the corresponding spectra presented in Fig. S3(e–f). The pristine GCS exhibited characteristic peaks: a D band at 1350 cm^{-1}, indicative of disordered sp^3 carbon structures, and a G band at 1580 cm^{-1}, corresponding to graphitic sp^2 carbon structures, both attributed to C-C bond stretching vibrations [6]. When MnO_2 was deposited onto the GCS surface, the intensities of the D and G bands diminished significantly or were no longer detectable. This attenuation is attributed to the shielding effect of the MnO_2 coating, which suppressed the Raman response from the underlying carbon substrate. Concurrently, a prominent peak emerged at 634 cm^{-1} in the spectra of the GCS@MnO_2-x catalysts. This peak is assigned to the symmetric stretching vibration of the O-Mn-O bond within δ-MnO_2, a finding consistent with the XRD phase analysis, thereby confirming the successful loading of MnO_2 and the formation of a crystalline structure. Furthermore, the force constant (k) of the Mn-O bond was calculated from the Raman data based on Hooke's law [7]. The derived k values exhibited a decreasing trend in the order: GCS@MnO_2-2 > GCS@MnO_2-4 > GCS@MnO_2-10 > GCS@MnO_2-8 > GCS@MnO_2-6. Theoretical studies indicate that a reduction in the Mn-O bond force constant signifies a weakened bond strength, which facilitates lattice oxygen activation. Consequently, the diminished vibrational characteristics of the Mn-O bond in GCS@MnO_2-6 correlate with a significant enhancement in lattice oxygen reactivity, leading to improved charge mobility and overall redox performance of the catalyst [7].

Fourier transform infrared (FTIR) spectroscopy was employed to analyze the chemical structure of the GCS@MnO_2-x catalysts, with the corresponding spectra presented in Fig. S3(g–h). Its main characteristic peaks are distributed in the following regions: 4000–3400 cm^{-1} (bending vibration of O-H groups), 2000–1610 cm^{-1} (stretching vibration of the G-band of graphite carbon C-C bonds), 1580–1300 cm^{-1} (disordered carbon structure of the D-band), 762 cm^{-1} and 508 cm^{-1} (lattice vibration of Mn-O), and 434 cm^{-1} (vibration of Mn-C bonds). The O-H peak originates from hydroxyl groups adsorbed on the catalyst surface. The double peaks at 2000–1610 cm^{-1} and 1580–1300 cm^{-1} correspond to the sp^2 and sp^3 hybridization characteristics of graphitic carbon, respectively. Critically, the distinct Mn-C bond peak at 434 cm^{-1} [8] confirms chemical bonding at the GCS/MnO_2 interface, providing direct evidence for successful core-shell structure formation. Furthermore, the GCS@MnO_2-6 sample exhibited significantly higher intensities for both Mn-O and Mn-C vibrations compared to other loadings, indicating enhanced interfacial bonding and metal-support interactions. This finding aligns with prior XRD and TEM characterization results.

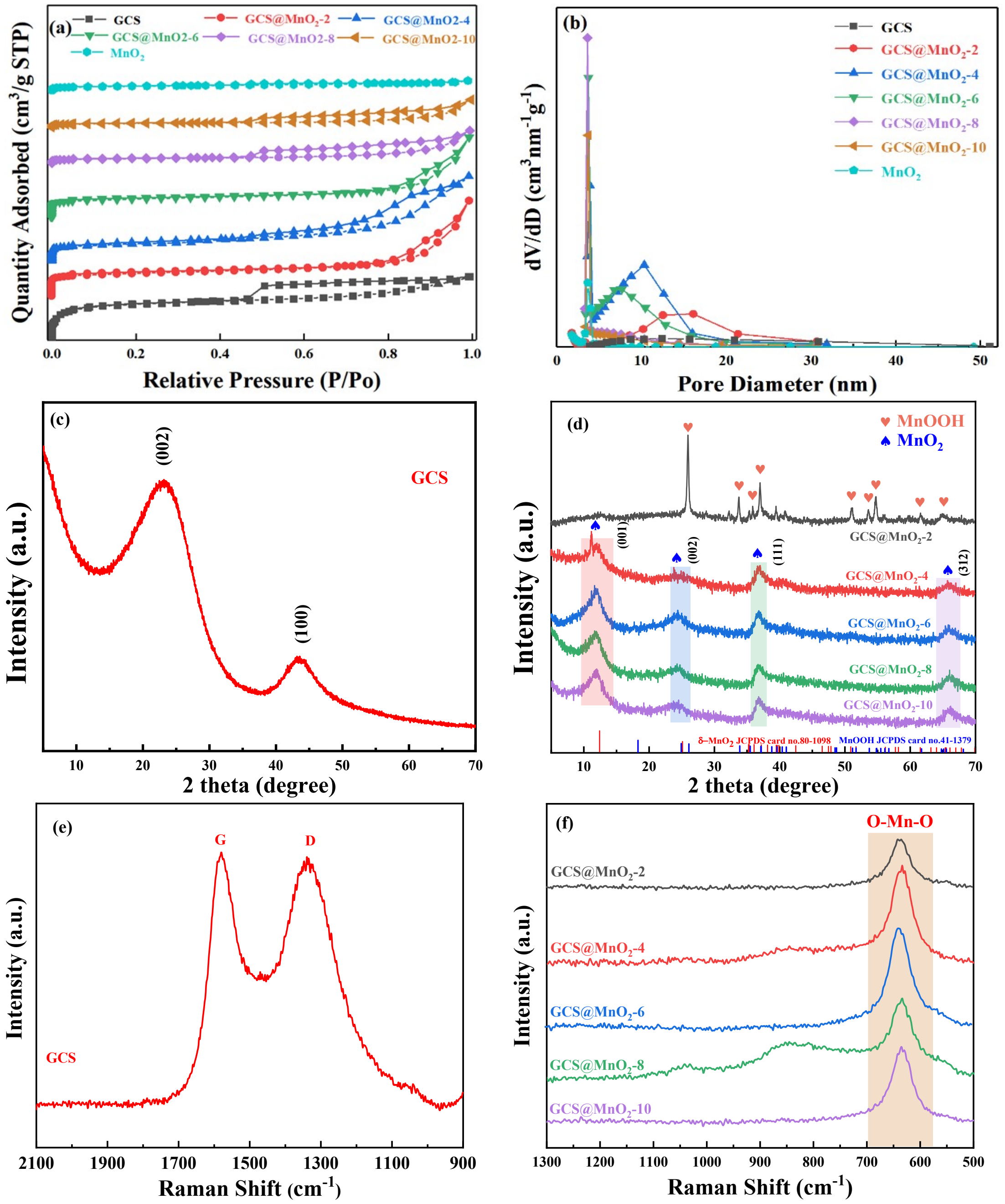

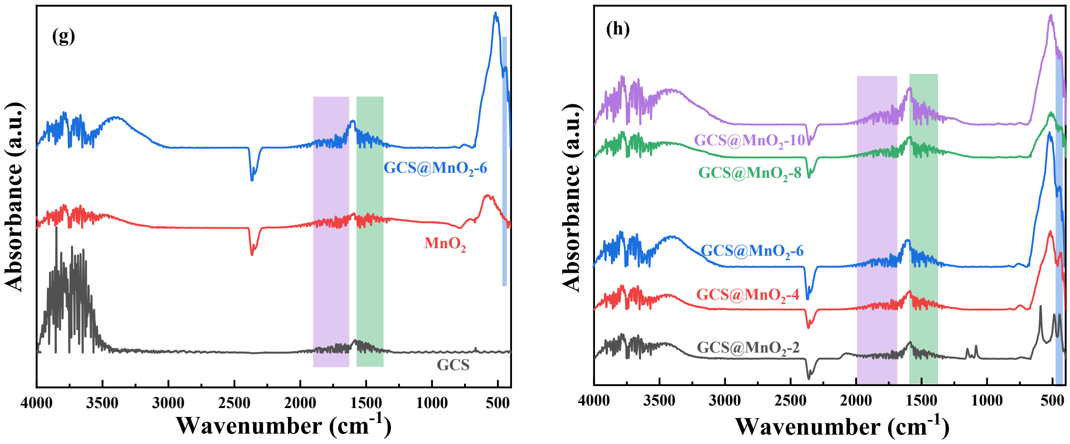

Fig. S3 Characterization of GCS@MnO$_2$-x catalyst: (a) N_2 adsorption-desorption isotherms; (b) Pore size distribution; (c) XRD pattern of GCS; (d) XRD pattern of GCS@MnO$_2$-x; (e) Raman spectrum of GCS; (f) Raman spectrum of GCS@MnO$_2$-x; (g) FTIR spectra of GCS, MnO$_2$ and GCS@MnO$_2$-6; (h) FTIR spectrum of GCS@MnO$_2$-x

Table S1 Structural parameters of GCS@MnO$_2$-x catalyst

catalyst	S_{BET}（m^2g^{-1}）[a]	V_{pore}（cm^3g^{-1}）[b]	Pore size（nm）[c]
GCS	522.91	0.19	11.50
GCS@MnO$_2$-2	242.26	0.46	18.87
GCS@MnO$_2$-4	216.32	0.50	9.46
GCS@MnO$_2$-6	171.15	0.37	7.86
GCS@MnO$_2$-8	57.92	0.16	7.06
GCS@MnO$_2$-10	47.56	0.15	7.73

[a] Specific surface area is determined by the linear part of the BET equation (P/P_o = 0.05-0.30);

[b] Total adsorption pore volume calculated by the BJH method when P/P_o = 0.995;

[c] Average pore diameter calculated by the BJH method during the desorption stage.

XPS analysis of GCS@MnO_2-x (Fig. S4a) confirms the coexistence of Mn, O, and C elements via distinct Mn 2p, O 1s, and C 1s peaks. Deconvolution of the C 1s spectrum (Fig. S4b) identifies three peaks: a dominant graphitic carbon (C–C/C=C) signal at 284.8 eV, with secondary peaks at 286.2 eV (C=O) and 289.1 eV (O–C=O), the latter two potentially arising from moisture adsorption [9, 10]. The O 1s spectrum (Fig. S4c) resolves lattice oxygen (O_{lat}, Mn–O, 529.8 eV), adsorbed oxygen (O_{ads}, surface hydroxyl/vacancy-derived, 531.3 eV), and adsorbed water-related C–O (533.6 eV) [4]. Notably, GCS@MnO_2-6 exhibits an O_{ads}/O_{lat} ratio of 82.27% (Table S2), significantly exceeding other catalysts, correlating with enhanced low-temperature toluene oxidation activity [11]. The Mn 2p spectrum (Fig. S4d) reveals Mn^{2+} (641.0 eV), Mn^{3+} (642.3 eV), and Mn^{4+} (643.5 eV) states. A strong positive correlation exists between the $(Mn^{2+}+Mn^{3+})/Mn^{4+}$ and O_{ads}/O_{lat} ratios. GCS@MnO_2-6 shows the highest $(Mn^{2+}+Mn^{3+})/Mn^{4+}$ ratio (2.11), confirming surface dominance by low-valence Mn. It is worth noting that the binding energies of Mn^{3+} and Mn^{4+} in GCS@MnO_2-6 are shifted towards lower energy by about 0.2–0.3 eV compared with other samples, which is attributed to the increase in the electron cloud density of the Mn 3d orbital. This indicates that electrons are transferred from the GCS support to the Mn metal, confirming the enhanced metal-support electronic interaction [12]. The high Mn^{3+} proportion further signifies abundant oxygen vacancies [13], while the elevated $(Mn^{2+}+Mn^{3+})/Mn^{4+}$ ratio promotes Mn–O bond cleavage and oxygen species participation in toluene oxidation [14, 15].

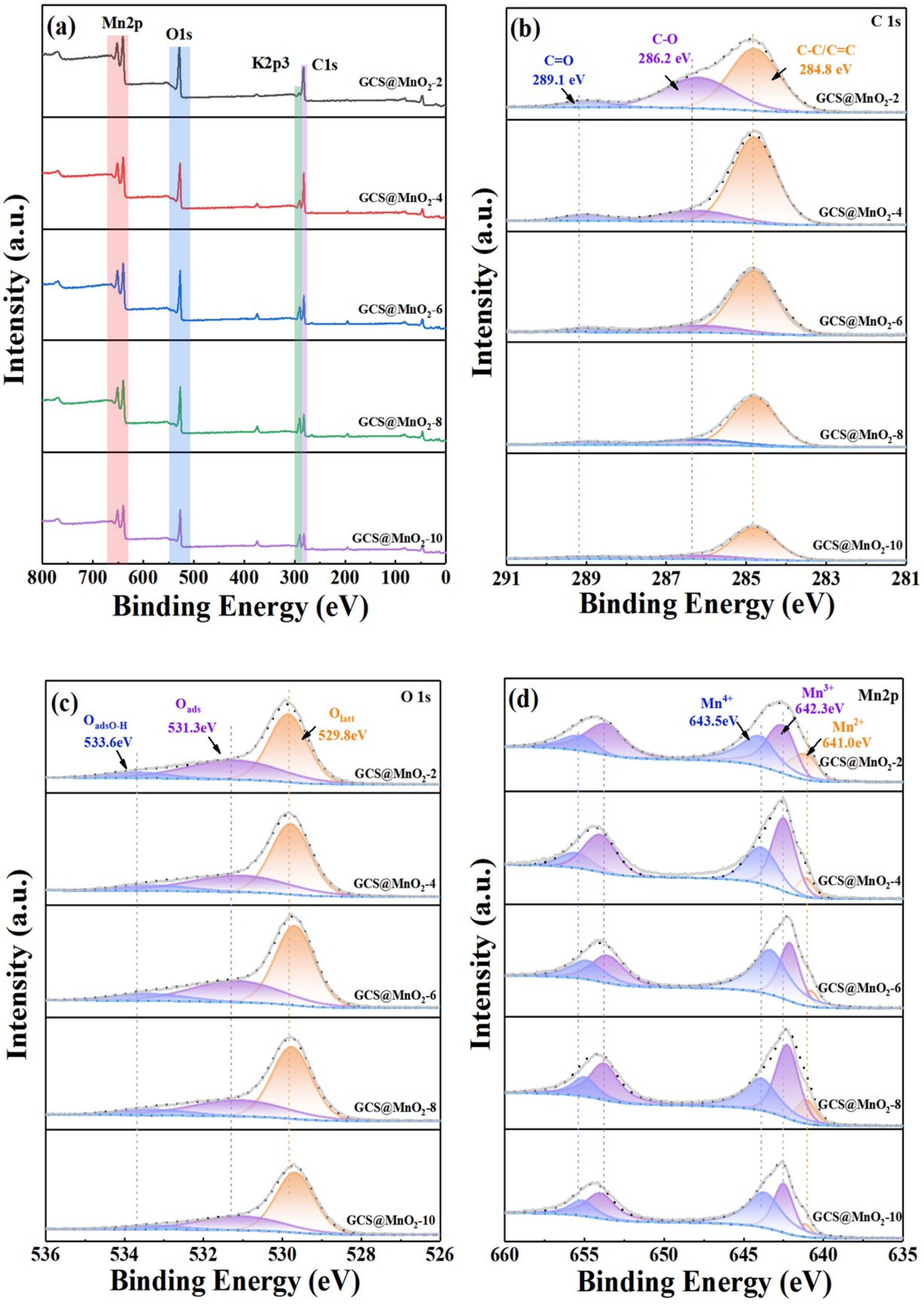

Fig. S4 XPS spectra of GCS@MnO$_2$-x catalysts: (a) Survey spectrum; (b) Mn 2p; (c) O 1s; (d) C 1s

Table S2 Surface elemental composition of GCS@MnO_2-x

Sample	Mn2p[a]			(Mn^{2+}+Mn^{3+})/Mn^{4+}	O1s[a]			O_{ads}/O_{lat}
	Mn^{2+}	Mn^{3+}	Mn^{4+}		O_{lat}	O_{ads}	$O_{adsO\text{-}H}$	
GCS@MnO_2-2	15.29	41.57	43.14	1.31	56.95	31.02	12.03	0.55
GCS@MnO_2-4	10.13	46.27	43.60	1.29	54.82	31.48	13.70	0.57
GCS@MnO_2-6	9.25	58.59	32.16	2.11	45.10	37.12	17.78	0.82
GCS@MnO_2-8	12.64	50.83	36.53	1.74	51.90	34.69	13.41	0.67
GCS@MnO_2-10	13.57	49.06	37.37	1.67	52.47	34.22	13.37	0.65

[a] The element ratios of Mn, O, and C are calculated from the peak area.

The redox properties of the GCS@MnO_2-x catalysts were systematically evaluated using H_2-TPR and O_2-TPD techniques. H_2-TPR spectra （Fig. S5a） revealed weak reduction peaks below 200 °C for all samples, attributed to the reduction of surface chemisorbed oxygen species (O_{ads}) [16]. Quantitative integral (Table S3) confirms that GCS@MnO_2-6 had the largest peak area in this region, indicating the highest surface O_{ads} concentration [17]. This result was consistent with the trend of the O_{ads}/O_{lat} ratio in the XPS characterization. In the 200–400 °C range, the reduction peaks correspond to sequential MnO_2 reduction ($Mn^{4+} \rightarrow Mn^{3+} \rightarrow Mn^{2+}$) through $MnO_2 \rightarrow Mn_2O_3 \rightarrow MnO$ phase transitions. Notably, GCS@MnO_2-6 displayed three distinct reduction peaks at 253, 270, and 291 °C within this range. Compared to GCS@MnO_2-10, the peak positions for GCS@MnO_2-6 were uniformly shifted to lower temperatures, indicating its enhanced reducibility. Calculation of the H_2-TPR curve integral areas revealed the following order of H_2 consumption: GCS@MnO_2-6 > GCS@MnO_2-10 > GCS@MnO_2-2. GCS@MnO_2-6 consumed the most H_2, signifying its highest content of reducible oxygen species (primarily O_{ads}). Thus, GCS@MnO_2-6 demonstrates optimal catalytic activity, attributable to its superior low-temperature reducibility, significantly enhanced surface oxygen mobility, and high density of oxygen vacancies [18].

The distribution of surface active oxygen species on GCS@MnO_2-x catalysts was investigated using O_2-TPD, with results presented in Fig. S5(b). Complementary O_2-TPD results delineate oxygen speciation: chemisorbed oxygen (100–300 °C), lattice oxygen (300–600 °C), and bulk lattice oxygen (>600 °C) [18]. Consistent with established principles [19], physically/chemically adsorbed oxygen species exhibit higher desorption ease than lattice oxygen. Within the 200–300 °C range, GCS@MnO_2-6 demonstrates significantly higher oxygen desorption capacity than other catalysts, confirming its maximal surface O_{ads} concentration. In the 300–600 °C region, GCS@MnO_2-6 shows the most intense desorption peak, indicating substantially enhanced O_{lat} mobility attributed to oxygen vacancy enrichment [19]. Structural variations among GCS@MnO_2-x catalysts lead to distinct O_2 desorption behaviors, with total desorption capacities following the order: GCS@MnO_2-6 > GCS@MnO_2-10 > GCS@MnO_2-2. By calculating the integral area of the O_2-TPD curve (Table S2), it was found that GCS@MnO_2-6 had the largest O_2 desorption amount and a lower secondary desorption peak temperature, proving that this catalyst had excellent oxygen activation ability and high oxygen mobility [16].

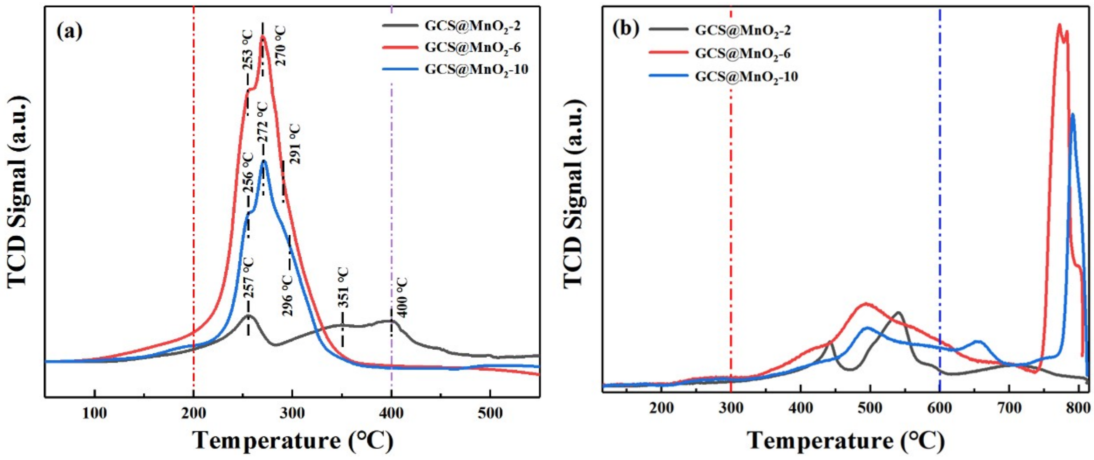

Fig. S5 Redox properties of GCS@MnO_2-x: (a)H_2-TPR; (b)O_2-TPD

Table S3 H_2-TPR andO_2-TPD calculation of GCS@MnO_2-x

catalyst	GCS@MnO_2-2	GCS@MnO_2-6	GCS@MnO_2-10
H_2 consumption (mmol·g^{-1})[a]	0.37	1.56	0.69
O_2 consumption (mmol·g^{-1})[b]	0.73	1.60	1.19

[a] The consumption of H_2 is calculated from the peak area.

[b] The consumption of H_2 is calculated from the peak area.

The light absorption performance of the GCS@MnO_2-x catalysts was characterized by ultraviolet-visible diffuse reflectance spectroscopy (UV-vis DRS), and the results are shown in Fig. S6(a). Due to the black nature of the GCS@MnO_2-x catalysts, all GCS@MnO_2-x catalysts exhibited good light absorption ability in the entire spectral range. Further analysis showed that the light absorption performance of the series of catalysts was in the order of: GCS@MnO_2-6 > GCS@MnO_2-8 > GCS@MnO_2-10 > GCS@MnO_2-4 > GCS@MnO_2-2. Notably, GCS@MnO_2-6 had the highest light absorption intensity in the ultraviolet-visible region, and it was inferred that it had the best performance in absorbing ultraviolet-visible light and the highest light utilization rate [20].

The valence band positions (E_{VB}) of the GCS@MnO_2-x catalyst series were calculated using the formula $E_{VB}=E_{CB}+E_g$, yielding the following values: GCS@MnO_2-2 (1.38 eV), GCS@MnO_2-4 (1.68 eV), GCS@MnO_2-6 (2.00 eV), GCS@MnO_2-8 (2.03 eV), GCS@MnO_2-10 (2.06 eV). As illustrated in Fig. S6(b), the conduction band energy (E_{CB}) of all catalysts lies below the oxygen reduction potential（$O_2/\cdot O_2^-$，-0.33 eV vs NHE）. This indicates that photogenerated electrons(e^-) possess sufficient driving force to reduce adsorbed oxygen (O_2) to superoxide radicals ($\cdot O_2^-$) [20, 21]. Furthermore, the E_{VB} values of GCS@MnO_2-6, GCS@MnO_2-8, and GCS@MnO_2-10 exceed the water oxidation potential （H_2O/OH^-，1.99 eV vs NHE）, enabling photogenerated holes （h^+） to efficiently oxidize H_2O or surface hydroxyl groups (OH^-) to hydroxyl radicals ($\cdot OH$) [22]. Concurrently, photoexcitation generates a localized thermal effect that synergistically enhances photogenerated carrier separation by reducing the migration barrier, thereby promoting reactive oxygen species (ROS) generation [23]. Chronoamperometry (i-t curves) was employed to evaluate carrier separation efficiency (Fig. S6c). The steady-state photocurrent density follows the order: GCS@MnO_2-6 > GCS@MnO_2-8 > GCS@MnO_2-10 > GCS@MnO_2-4 > GCS@MnO_2-2. Higher photocurrent values correlate with lower electron-hole recombination rates and enhanced interfacial charge transfer efficiency [24]. The significantly stronger photocurrent response of GCS@MnO_2-6 confirms its superior carrier separation capability. Consistent with prior XPS and EPR results, high-density oxygen vacancies in GCS@MnO_2-6 act as electron traps, suppressing carrier recombination and thus boosting photocatalytic oxidation performance.

Electrochemical impedance spectroscopy (EIS) characterization (Fig. S6d) revealed the charge transfer resistance (R_{ct}), with the Nyquist plot arc radius decreasing in the order: GCS@MnO_2-2 > GCS@MnO_2-4 > GCS@MnO_2-10 > GCS@MnO_2-8 > GCS@MnO_2-6. According to semiconductor electrochemical theory, a smaller arc radius indicates lower interfacial charge transfer resistance and higher carrier separation/transfer efficiency [25]. The minimal R_{ct} value of GCS@MnO_2-6 further validates its optimal separation and conversion efficiency for photogenerated electrons and holes [23]. Integrating photocurrent and XPS data, the enhanced charge separation in GCS@MnO_2-6 originates from rapid carrier migration, ultimately elevating its photothermal catalytic oxidation performance.

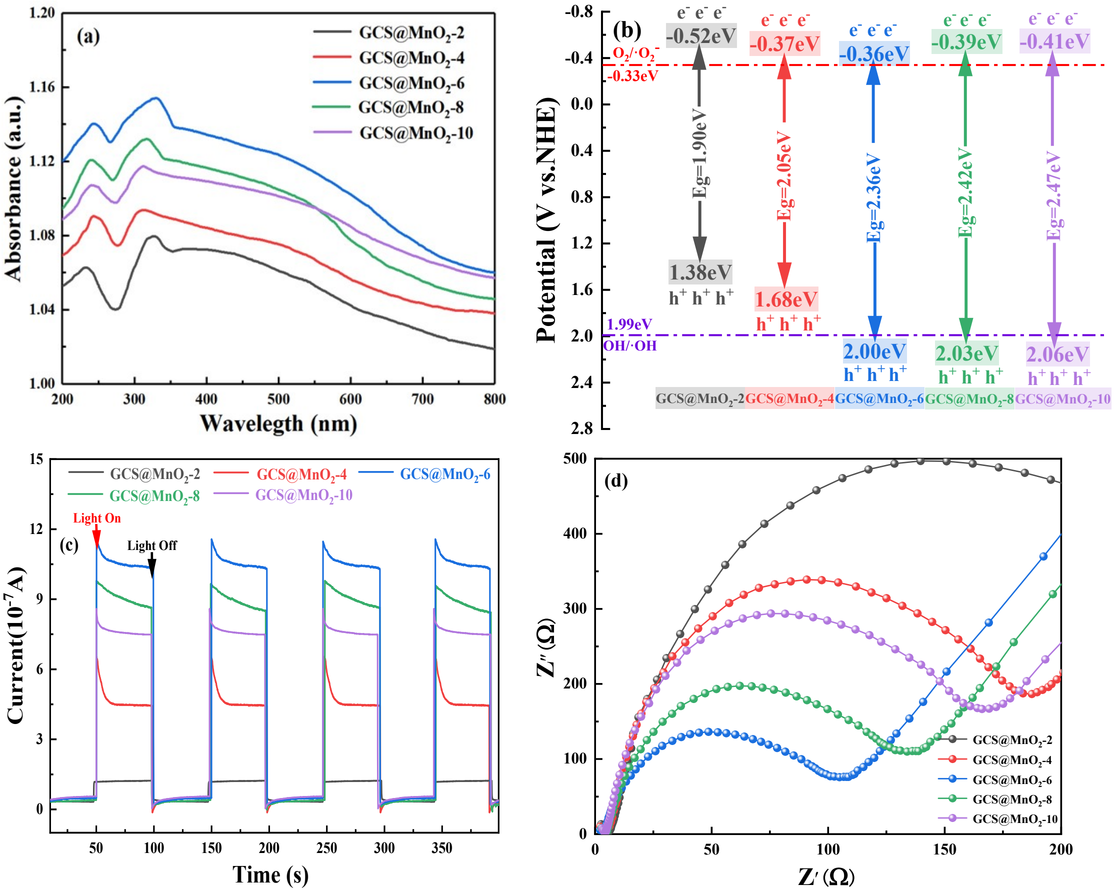

Fig. S6 Photochemical properties of GCS@MnO_2-x catalyst: (a) UV-vis DRS diffuse reflectance spectrum; (b) Band gap structure; (c) Transient photocurrent response curve; (d) EIS Nyquist plot

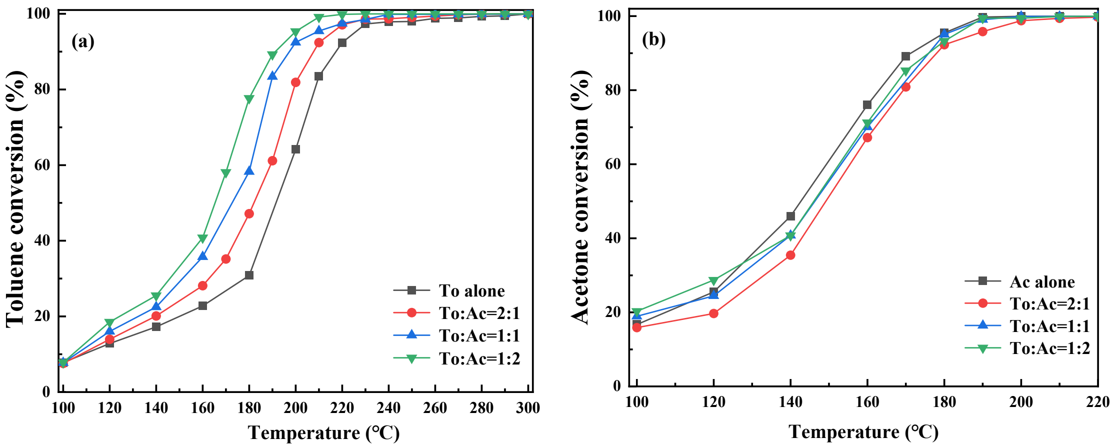

Fig. S7 Conversion of toluene and acetone by GCS@MnO$_2$ in TCO system: (a) Toluene conversion; (b) Acetone conversion

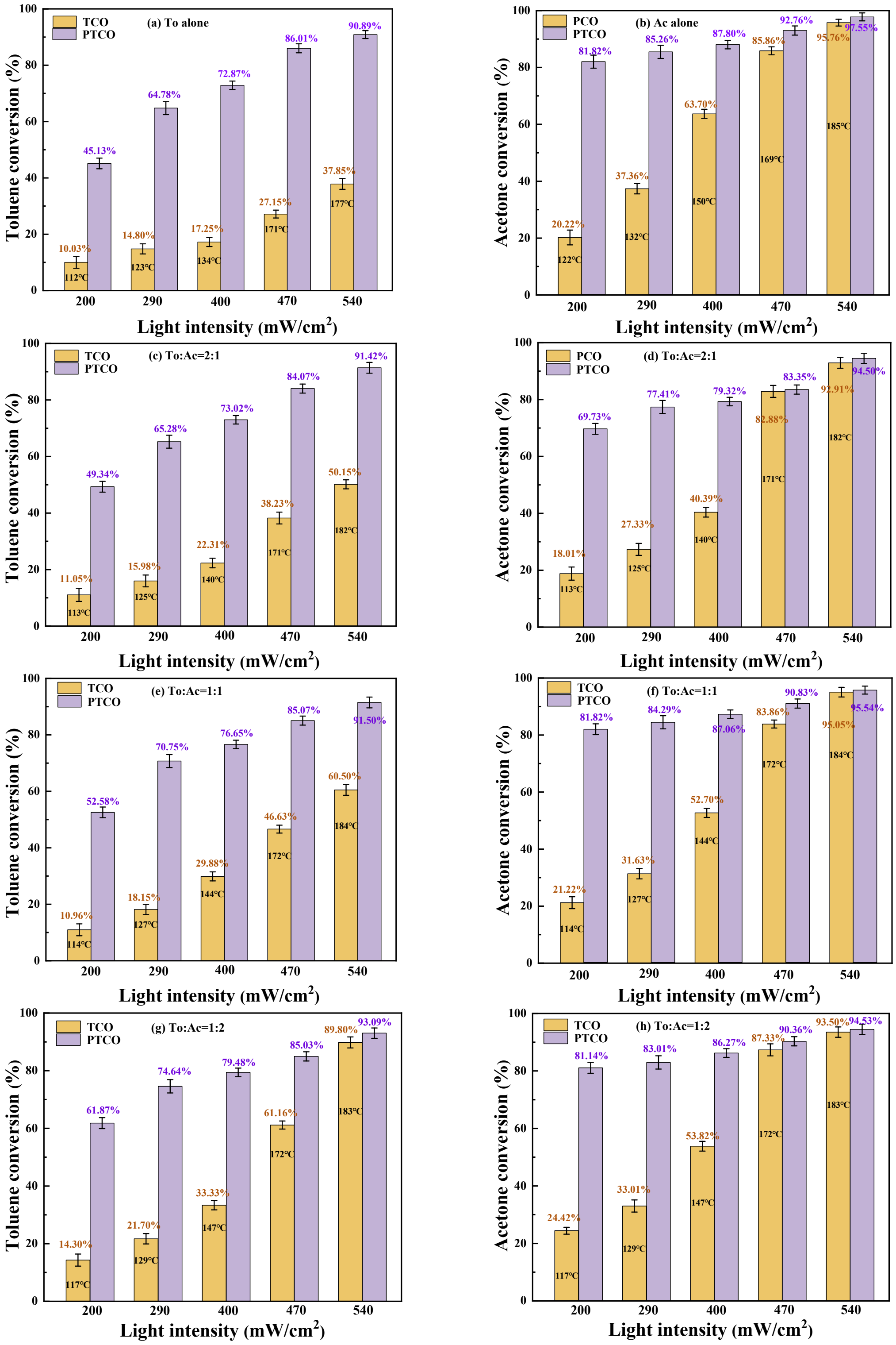

Fig. S8 The comparison the toluene and acetone oxidation between the PTCO and the TCO systems

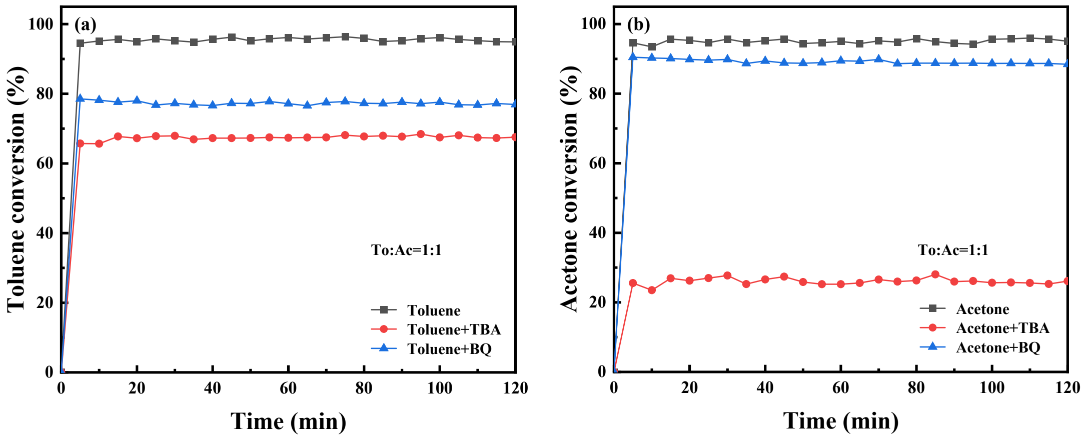

Fig. S9 The radical quenching experiments for GCS@MnO_2 at light intensity of 540 mW/cm^2: (a) Toluene conversion; (b) Acetone conversion

Table S4 The apparent activation energy and turnover frequency of toluene/acetone oxidation over GCS@MnO_2

Reaction		Fitting equation	Ea (kJ/mol)	A×10^5 (ml·g^{-1} ·min^{-1})	R^2	TOF[a]×10^{-5} (s^{-1})
Toluene oxidation	To alone	y=-3.16x+14.11	26.30	13.42	0.93	2.22
	(To:Ac=2:1)	y=-2.92x+13.50	24.28	7.26	0.95	2.24
	(To:Ac=1:1)	y=-2.68x+12.97	22.28	4.29	0.92	2.24
	(To:Ac=1:2)	y=-2.34x+12.24	19.46	2.08	0.91	2.28
Acetone oxidation	Ac alone	y=-2.04x+11.87	16.97	1.43	0.90	2.39
	(To:Ac=2:1)	y=-2.07x+11.78	17.24	1.31	0.98	2.32
	(To:Ac=1:1)	y=-1.39x+10.30	11.54	2.97	0.89	2.34
	(To:Ac=1:2)	y=-1.40x+10.27	11.61	2.88	0.92	2.31

[a] The TOF was calculated based on surface Mn atoms measured by XPS.

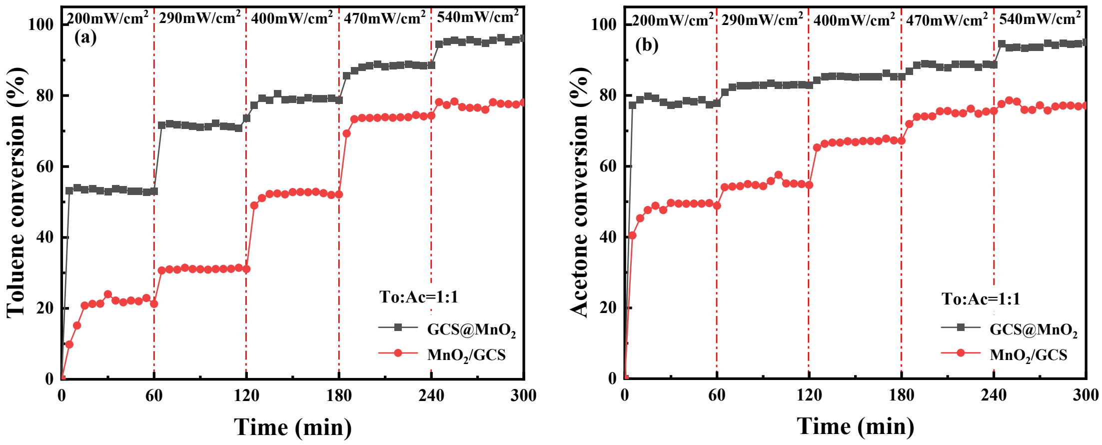

Fig. S10 Photothermal catalytic co-oxidation of toluene and acetone by GCS@MnO$_2$ and MnO$_2$/GCS: (a) Toluene conversion; (b) Acetone conversion

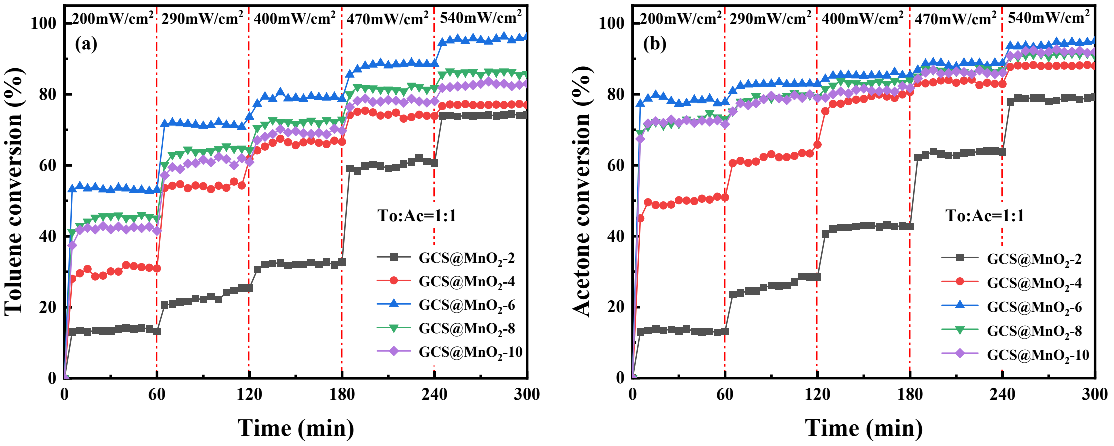

Fig. S11 The conversion of toluene and acetone over GCS@MnO$_2$-x in PTCO system: (a)Toluene conversion; (b) Acetone conversion

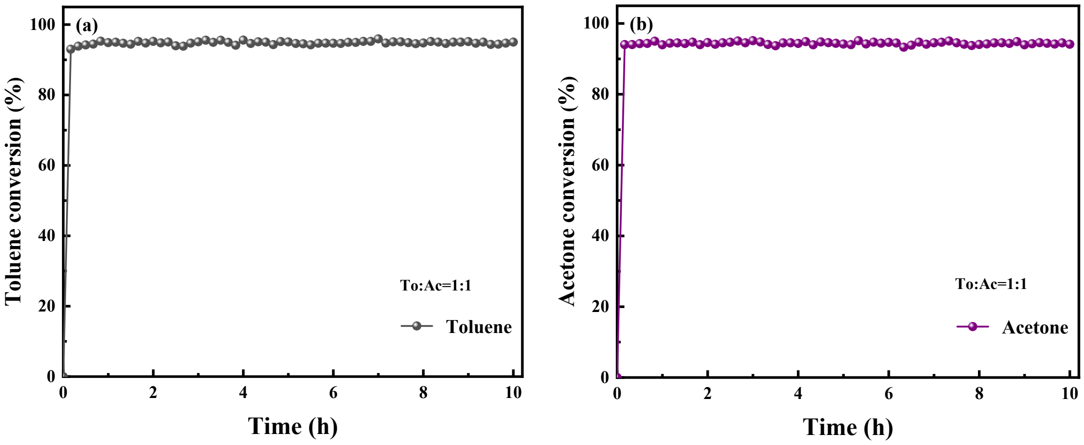

Fig. S12 Stability test of photothermal catalytic oxidation of toluene and acetone on GCS@MnO_2

Table S5 Comparison of VOCs oxidation by different catalysts in PTCO system

Catalyst	Target VOCs	Temperature (°C)	light intensity (mW/cm^2)	Conversion rate	WHSV ($mL\cdot g^{-1}\cdot h^{-1}$)	Reference
$CuMn_2O_4/Mn_2O_3$	toluene	233	700	90	30000	[13]
α-$MnO_2/CeMnO_3$	toluene	201	550	90	30000	[26]
20CuO_x-WO_x/mTiO_{2-x}-USY	toluene	235	500	90.4	30000	[27]
Pt-Co_{20}/CN	toluene	183	500	90	30000	[28]
Cu/CeO_2	toluene	231	529	90	30900	[29]
Co_3O_4–M-4	ethyl acetate	200	910	90	30000	[30]
$La_{0.9}Fe_{0.1}MnO_3$	toluene	208	1340	90	30000	[31]
GCS@MnO_2	toluene & acetone	184	540	95 & 94	30000	This work

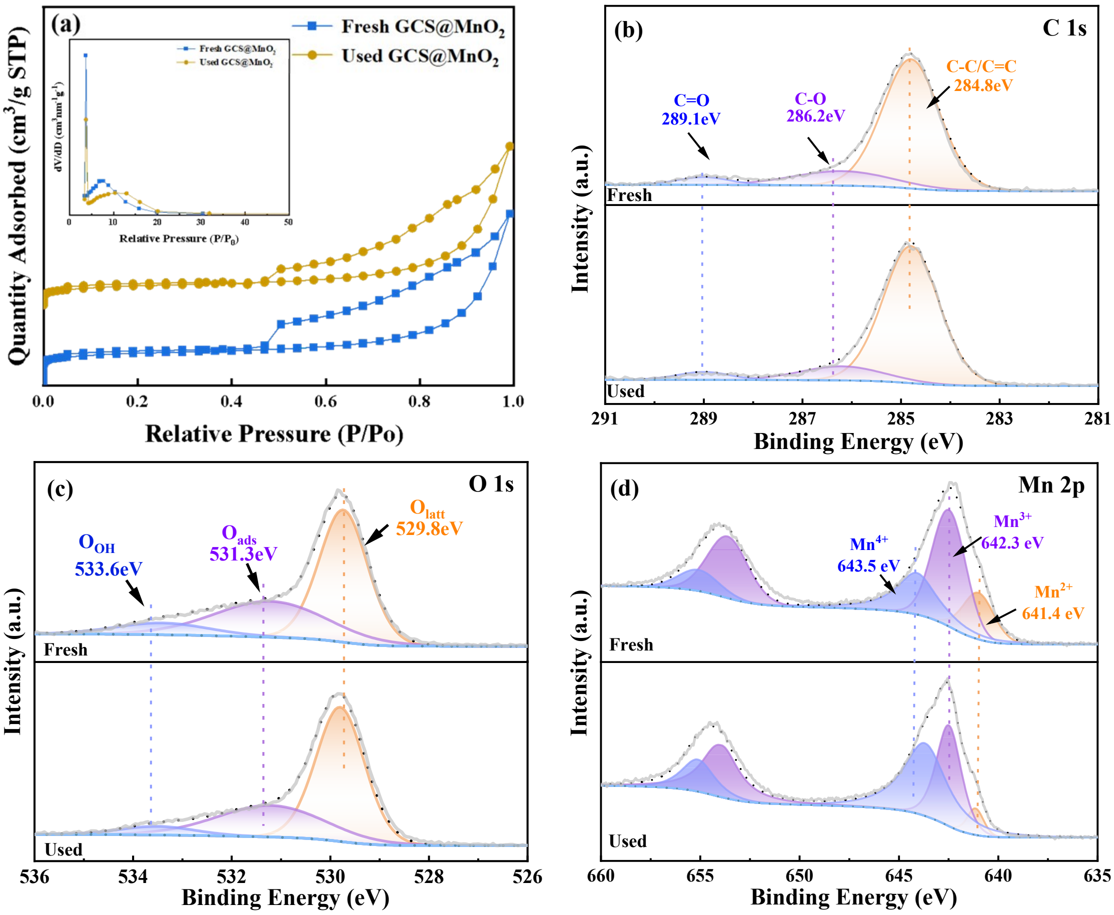

Fig. S13 The physicochemical properties of the fresh and used GCS@MnO$_2$: (a) BET; (b) XPS

Table S6 Physicochemical parameters of fresh and used GCS@MnO$_2$

Sample	S_{BET}^{a} (m^{2}g^{-1})	V_{pore}^{b} (cm^{3}g^{-1})	Pore size^c (nm)	Mn2p^d			(Mn^{2+}+Mn^{3+})/Mn^{4+}	O1s^d			O_{ads}/O_{lat}
				Mn^{2+}	Mn^{3+}	Mn^{4+}		O_{lat}	O_{ads}	$O_{adsO\text{-}H}$	
Fresh	171.15	0.37	7.86	9.25	58.59	32.16	2.11	45.10	37.12	17.78	0.82
Used	165.89	0.36	8.15	8.33	57.36	34.31	1.91	48.32	39.36	12.37	0.81

[a] Specific surface area is determined by the linear part of the BET equation (P/P_0 = 0.05-0.30);

[b] Total adsorption pore volume calculated by the BJH method when P/P_0 = 0.995;

[c] Average pore diameter calculated by the BJH method during the desorption stage.

[d] The contents of Mn and O are determined by calculation based on the fitting results of XPS peak areas.

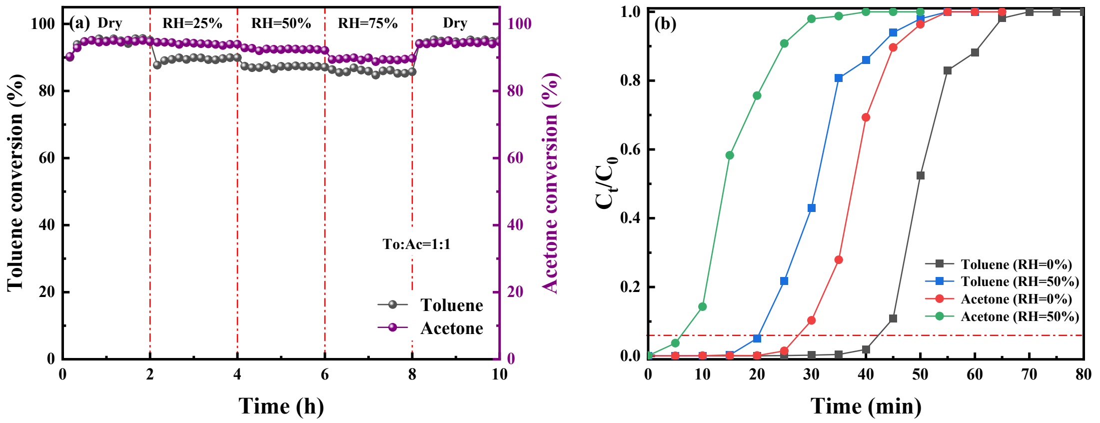

Fig. S14 Effect of humidity on conversion of toluene and acetone in PTCO system: (a) Co-oxidation of toluene and acetone on GCS@MnO_2; (b) Effect of humidity on adsorption of toluene or acetone

References:

[1] Y. Zhang, Y. Zhu, Y. Fan, Z. Zhu, L. Liao, S. Mo, L. Zhang, S. Tang, X. Zhou. Highly active nanostick-assembled $TiO_2@MnO_x$ hollow-sphere structure for photothermocatalysis of ethyl acetate and NO with free-ammonia at low temperature: Resistence, key reaction steps and mechanisms, Applied Surface Science, 607 (2023) 154887.

[2] M. Li, Y. Wang, Y. Fan, L. Liao, X. Zhou, S. Mo, H. Wang. Controllable synthesis various morphologies of 3D hierarchical MnO_x-TiO_2 nanocatalysts for photothermocatalysis toluene and NO with free-ammonia, Journal of Colloid and Interface Science, 608 (2022) 3004-3012.

[3] Y. Shu, Y. Xu, H. Huang, J. Ji, S. Liang, M. Wu, D. Y.C. Catalytic oxidation of VOCs over Mn/TiO_2/activated carbon under 185 nm VUV irradiation, Chemosphere, 208 (2018) 550-558.

[4] Y. Wang, X. Li, J. He, J. Xiao, D. Chen, N. Li, Q. Xu, H. Li, J. Lu. Manganese dioxide supported on hollow graphitized carbon spheres for the catalytic oxidation of toluene: Improved adsorption and electron transfer, Separation and Purification Technology, 321 (2023) 124203.

[5] T. Zhang, B. Li, C. Wang, S. Wu, S. Zhu, H. Jiang, Y. Zheng, Z. Li, Z. Cui, Y. Zhang, P. Chu, X. Liu. Tunning the bandgap of MnO_2 homojunction by building active high-index facet to achieve rapid electron transfer for enhanced photocatalytic sterilization, Journal of Materials Science & Technology, 168 (2024) 265-275.

[6] M. Yadav, A. Pophali, N. Verma, T. Kim. Oxidation of VOCs on a highly stabilized furfuryl alcohol-based activated carbon supported nickel oxide catalyst, Journal of Industrial and Engineering Chemistry, 105 (2022) 313-323.

[7] B. Chang, L. Tang, X. Zhang, J. Li, Z. Shen, J. Lyu. Optimization of photothermal

conversion and catalytic sites for photo-assisted-catalytic degradation of volatile organic compounds, Chemosphere, 310 (2023) 136696.

[8] J. Wang, X. Gao, Y. Wang, S. Wang, Z. Xie, B. Yang, Z. Zhang, Z. Yang, L. Kang, W. Yao. Multifunctional core-double-shell C@MnO@TiO_2 catalysts with enhanced full-light conversion for the highly efficient photothermal oxidation of toluene, Applied Catalysis B: Environmental, 317 (2022) 121789.

[9] M. Wang, X. Hong, J. Chen, J. Li, X. Chen, J. Mi, Z. Liu, S. Xiong. Two-step hydrothermal synthesis of highly active MnO_x-CeO_2 for complete oxidation of formaldehyde, Chemical Engineering Journal, 440 (2022) 135854.

[10] S. Jiang, C. Li, Y. Muhammad, Y. Tang, R. Wang, J. Li, J. Li, Z. Zhao, Z. Zhao. Solvent-induced fabrication of Cu/MnOx nanosheets with abundant oxygen vacancies for efficient and long-lasting photothermal catalytic degradation of humid toluene vapor, Applied Catalysis B: Environmental, 328 (2023) 122509.

[11] W. B. Soltan, J. Peng, Z. Cao, Z. Fu, H. Liu. Bimetallic Fe-Mn loaded H-ZSM-5 zeolites for excellent VOCs catalytic oxidation at low-temperatures: Synergistic effects and catalytic mechanisms, Chemical Engineering Journal, 475 (2023) 146251.

[12] J. Su, Q. Ke, H. Xu. Hierarchically MnO_2/SiO_2 nanocomposites with high solar light-driven photo-thermo catalysis activity for efficient toluene removal, Applied Surface Science, 608 (2023) 155177.

[13] L. Nie, S. Li, S. Chai, N. Han, Y. Chen. Photothermal catalytic oxidation of toluene with enhanced efficiency over constructed $CuMn_2O_4/Mn_2O_3$ heterojunction catalyst, Applied Surface Science, 605 (2022) 154567.

[14] Y. Wang, J. Dai, M. Wang, F. Qi, X. Jin, L. Zhang. Enhanced toluene oxidation by photothermal synergetic catalysis on manganese oxide embedded with Pt single-atoms, Journal of Colloid and Interface Science, 2023, 636: 577-587.

[15] J. Chen, D. Yan, Z. Xu, X. Chen, X. Chen, W. Xu, H. Jia, J. Chen. A Novel Redox Precipitation to Synthesize Au-Doped α-MnO_2 with High Dispersion toward Low-Temperature Oxidation of Formaldehyde, Environ Sci Technol, 52 (2018) 4728-4737.

[16] X. Yao, J. Zhang, X. Liang, C. Long. Plasma-catalytic removal of toluene over the supported manganese oxides in DBD reactor: Effect of the structure of zeolites support, Chemosphere, 208 (2018) 922-930.

[17] M. Zhang, G. Li, Q. Li, J. Chen, E.A. Elimian, H. Jia, H. He. In Situ Construction of Manganese Oxide Photothermocatalysts for the Deep Removal of Toluene by Highly Utilizing Sunlight Energy, Environ Sci Technol, 57 (2023) 4286-4297.

[18] Y. Zeng, J. Zhong, F. Feng, D. Ye, Y. Hu. Synergistic photothermal catalytic oxidation of methanol and toluene mixture over Co-MOFs-derived catalyst: Interfacial and promotion effects, Chemical Engineering Journal, 485 (2024) 149720.

[19] J. Zhao, C. Li, Q. Yu, Y. Zhu, X. Liu, S. Li, C. Liang, Y. Zhang, L. Huang, K. Yang, Z. Zhang, Y. Zhai. Interface engineering of Mn_3O_4/Co_3O_4 S-scheme heterojunctions to enhance the photothermal catalytic degradation of toluene, Journal of Hazardous Materials, 452 (2023) 131249.

[20] Y. Wang, Y. Bi, G. Ji, Y. Jing, J. Zhao, E. Sun, Y. Wang, H. Chang, F. Liu. Acid-activated α-MnO_2 for photothermal co-catalytic oxidative degradation of propane: Activity and reaction mechanism, Journal of Hazardous Materials, 478 (2024) 135447.

[21] Y. Bi, G. Ji, E. Sun, C. Feng, F. Han, F. Liu, Y. Liu. In-situ modulation of α-MnO_2 surface oxygen vacancies for photothermal catalytic oxidation of propane: Insights into activity and synergistic mechanism, Chemical Engineering Journal, 473 (2023) 145474.

[22] J. Li, H. Zhang, J. Sun, H. Yang, J. Xiang, X. Zhang, S. Zhang. Photothermal synergistic catalytic oxidation mechanism of toluene by Ce-doped $SrTiO_3$ via one-pot hydrothermal synthesis, Applied Surface Science, 680 (2025) 161374.

[23] Z. Shayegan, F. Haghighat, C. Lee. Carbon-doped TiO2 film to enhance visible and UV light photocatalytic degradation of indoor environment volatile organic compounds, Journal of Environmental Chemical Engineering, 8 (2020) 104162.

[24] F. Bi, X. Zhang, J. Chen, Y. Yang, Y. Wang. Excellent catalytic activity and water resistance of UiO-66-supported highly dispersed Pd nanoparticles for toluene catalytic oxidation, Applied Catalysis B: Environmental, 269 (2020) 118767.

[25] L. Xu, P. Guo, J. Xu, B. Shen, S. Guo. Promoting the generation of hydroxyl radicals to improve the photocatalytic toluene oxidation: A combined strategy of morphology regulation and layered double hydroxide assistance, Separation and Purification Technology, 354 (2025) 128662.

[26] Y. Wang, S. Wang, Q. Liu, Y. Li, X. Hu, C. Wang, B. Liu. Photothermal catalytic oxidation of toluene over in-situ loaded α-MnO_2/$CeMnO_3$ catalyst, Colloids and Surfaces A: Physicochemical and Engineering Aspects, 726 (2025) 137974.

[27] E. A. Elimian, M. Zhang, Q. Li, J. Chen, Y. Sun, H. Jia, J. He. Light-driven photothermal catalytic oxidation of toluene over CuO_x-WO_x/mTiO_{2-x}-USY: Revealing CuO_x-WO_x synergy, Applied Catalysis B: Environmental, 331 (2023) 122702.

[28] M. Zhang, S. Cai, J. Li, E. Elimain, J. Chen, H. Jia. Ternary multifunctional catalysts of polymeric carbon nitride coupled with Pt-embedded transition metal oxide to enhance light-driven photothermal catalytic degradation of VOCs, J Hazard Mater, 412 (2021) 125266.

[29] Y. Zhang, M. Zhang, X. Lv, J. Chen, H. Jia. Maximum photoresponse in enhancing photothermocatalytic toluene oxidation: Modulation of Cu^+-O_v-Ce^{3+} and surface lattice oxygen via Cu/CeO_2 shape effect, Applied Catalysis B: Environment and Energy, 371 (2025) 125253.

[30] L. Huang, J. Zheng, S. Huang, J. Li, L. Liao, S. Mo. 2-methylimidazole-ligand-

induced geometric structure transformation of Co-MOFs-derived Co_3O_4 catalysts for enhanced focusing-light-driven photothermal VOC oxidation, Molecular Catalysis, 583 (2025) 115247.

[31] Q. Yu, C. Li, J. Zhao, X. Liu, L. Huang, Y. Zhu, K. Yang, Z. Zhang, D. Ma, Y. Zhang, Q. Huang. Efficient photothermal catalytic oxidation of toluene by $La_{1-x}Fe_xMnO_3$ with full spectrum response: The effects of Fe doping and photoactivation, Applied Catalysis B: Environmental, 327 (2023) 122441.